

# Understanding Vortex Ring Instability during Droplet Impact onto Thin Liquid Films Using High Speed PIV

Hatim Ennayar<sup>1,\*</sup>, Philipp Brockmann<sup>1</sup>, Juan Camilo Dueñas Torres<sup>1</sup>, Hyoungsoo Kim<sup>2</sup>, Jeanette Hussong<sup>1</sup>

1: Institute for Fluid Mechanics and Aerodynamics, Technical University of Darmstadt, Darmstadt, Germany

2: Department of Mechanical Engineering, Korea Advanced Institute of Science and Technology, Daejeon, Republic of Korea

\*Corresponding author: [ennayar@sla.tu-darmstadt.de](mailto:ennayar@sla.tu-darmstadt.de)

**Keywords:** Vortex ring instability, Droplet impact, Thin liquid film, Mixing, Crow instability, Elliptical instability.

## ABSTRACT

This study investigates vortex ring instability during droplet impact on thin liquid films using high-speed Particle Image Velocimetry (PIV) and Laser-Induced Fluorescence (LIF). Experiments were conducted using two different setups, capturing the droplet impact from both bottom and side views. The study examines how different dimensionless parameters (Reynolds number, Weber number and dimensionless thickness) influence vortex ring behavior in thin liquid films. Vortices were analyzed by identifying the centers using  $\Gamma_2$  scalar and calculating the vortex circulation through a two superposed Lamb-Oseen vortex fitting. The effect of film thickness on vortex dynamics reveals that thinner films lead to greater instability due to higher energy at the moment of wall collision, facilitating the formation of additional vortex structures. Experimental phase mapping highlights the critical threshold of Reynolds number  $Re$  and dimensionless thickness  $\delta$  for vortex ring instability. Moreover, the number of fingers formed due to vortex ring instabilities increases with higher Reynolds numbers and thinner films, providing a clear relationship between film thickness, impact energy, and the complexity of resulting fluid structures.

---

## 1. Introduction

The dynamics of droplet impact, particularly the formation and behavior of vortex rings, have garnered significant attention in fluid mechanics. Vortex rings are generated due to the azimuthal vorticity that arises from the high velocity gradients at the liquid-liquid interface immediately following impact (Cresswell & Morton, 1995), (Lee et al., 2015). These structures, which play a pivotal role in fluid dynamic processes, are influenced by the Reynolds number ( $Re$ ) and Weber number ( $We$ ) of the impact. As documented by Lee et al. (2015), higher  $Re$  and  $We$  values can lead to the formation of multiple vortex rings. This phenomenon significantly affects the ensuing flow dynamics and mixing.

Understanding the dynamics of vortex rings during droplet impact on thin liquid films is essential due to its implications in numerous applications, including coating processes, microfluidics, and

fuel injection systems, where efficient mixing and control over fluid behavior are crucial. Despite its importance, the behavior of vortex rings in thin liquid films have been relatively unexplored compared to deeper pools.

Previous studies have primarily focused on droplet impacts into deep pools (Saha et al., 2019), (Thoraval et al., 2016), (Lee et al., 2015), (Cresswell & Morton, 1995), (Peck & Sigurdson, 1994). These impacts can lead to the formation of up to four vortex rings as mentioned by Lee et al. (2015), with interactions such as the leapfrogging effect Shariff & Leonard (1992), Lim (1997b). During leapfrogging, the leading ring expands in size and slows down, while the trailing ring contracts, accelerates, and penetrates through the leading ring. This cyclic interaction continues until the two rings merge. Despite these interactions, the vortex rings usually maintain their circular shape as they descend into the pool as observed by Ennayar et al. (2023). Additionally, the azimuthal instabilities that develop during leapfrogging leave behind loop-like structures (Lim, 1997a).

In the context of thin liquid films, the interaction between the vortex ring and the substrate wall introduces unique dynamics. Observations by Ennayar et al. (2023) show that upon impact, the vortex ring undergoes radial stretching and forms a boundary layer near the wall. This interaction leads to flow separation and the creation of secondary vortex rings with opposite-signed vorticity. These secondary rings can exhibit azimuthal instabilities, which significantly affect the mixing efficiency.

Two primary types of instabilities influence vortex ring behavior: long-wavelength perturbations, known as Crow instability (Crow, 1970), and short-wavelength perturbations, referred to as Tsai-Widnall-Moore-Saffman (TWMS) instability or elliptical instability (Tsai & Widnall, 1976), (Moore & Saffman, 1975). At lower Reynolds numbers, Crow instability dominates the vortex-wall interaction dynamics. At higher Reynolds numbers, TWMS instability leads to the disintegration of the vortex ring into a turbulent cloud (Archer et al., 2010), (Cheng et al., 2010), (Harris & Williamson, 2012), (McKeown et al., 2020), (Mishra et al., 2021).

The goal of this study is to investigate the conditions under which these instabilities occur and to characterize the behaviors of vortex rings upon impacting the wall in thin liquid films. Given the lack of detailed research in this area, the current work aims to provide critical insights into the mechanisms driving vortex ring instabilities during droplet impact on thin liquid film. Particle Image Velocimetry (PIV) and Laser-Induced-Fluorescence (LIF), are utilized to enhance the understanding of Vortex ring-driven convective mixing processes and identify the critical parameters influencing these dynamics.

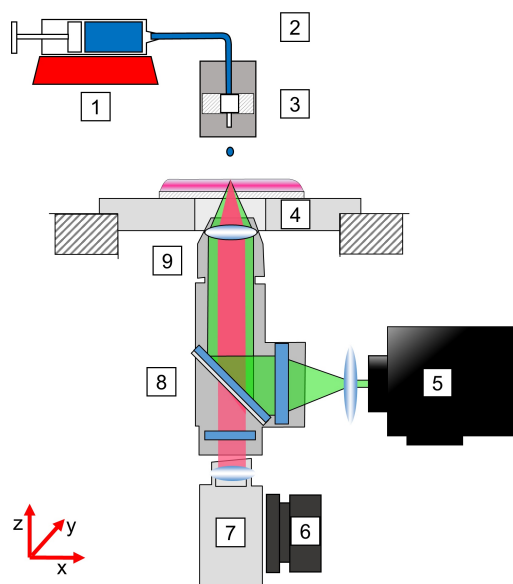


**Figure 1.** Schematic illustration of bottom view setup: (1) Syringe pump, (2) z-Travel, (3) Cannula, (4) Thin liquid film on FTO glass substrate, (5) High power LED, (6) x,y,z-Travel, (7) HS-Camera, (8) Dichroic mirror with bandpass filters, (9) Microscope Objective.

## 2. Experimental setup

The experimental setup for investigating the vortex ring dynamics and mixing efficiency during droplet impact on thin liquid films consists of two primary configurations: a bottom view setup (Fig. 1) and a side view setup (Fig. 2). Each configuration is designed to capture specific aspects of the impact process and consists of three principal components: Drop generator, impact substrate and an optical system.

The bottom view setup is designed to provide detailed observations of the droplet impact and subsequent mixing from below using the LIF technique (Ennayar et al., 2023). A precision syringe pump (Braun GmbH) drives a 5 mL syringe, connected via a tube to a blunt needle (Braun GmbH). This assembly is mounted on an automatically controlled traverse, allowing precise adjustments in drop height. A consistent flow rate is maintained to produce repeatable water droplets with diameters of  $D = 2.225 \pm 0.025$  mm and  $D = 3.9 \pm 0.025$  mm.

The impact substrate is a 50 mm × 50 mm glass plate (Sigma-Aldrich). The substrate is thoroughly cleaned with water and detergent, followed by immersion in an ultrasonic bath of isopropanol, granting an increase in surface energy for improved adhesion of the liquid film. Deionized water mixed with a fluorescent dye (Rhodamine B) is spread across the substrate. The film's thickness is adjusted by adding or removing small amounts of liquid using a syringe until the desired thickness is achieved. The initial film thickness is precisely measured with a chromatic-confocal point sensor (confocalDT IFS2407-0.8, Micro-epsilon) that offers an accuracy of  $\pm 0.4$   $\mu\text{m}$ . The sensor is mounted

on a motorized arm, enabling 3D scanning of the film thickness. The thicknesses  $h$  used are chosen to achieve a dimensionless thickness  $\delta = \frac{h}{D}$  ranging between 0.1 and 0.9.

The bottom view is captured using a custom-built microscope based on an optical tube (InfiniTube Special, Infinity Photo-Optical), illuminated by a 7 W high-power green LED ( $\lambda \approx 532$  nm, ILA iLA.LPS v3). The optical path includes a dichroic mirror and band-pass filters (Thorlabs DFM1/M) to direct light through the objective and filter the fluorescence signal. An Infinity Photo-Optical IF-3 objective lens with  $1\times$  magnification is used. High-speed imaging is performed with a 12-bit,  $2048\times 1952$  pixels CMOS camera (Phantom T1340, Vision Research). This setup provides a field of view of  $11.5\times 11.5$  mm<sup>2</sup>. The apparatus can be traversed in three dimensions with step sizes of  $1.25$   $\mu$ m for precise positioning.

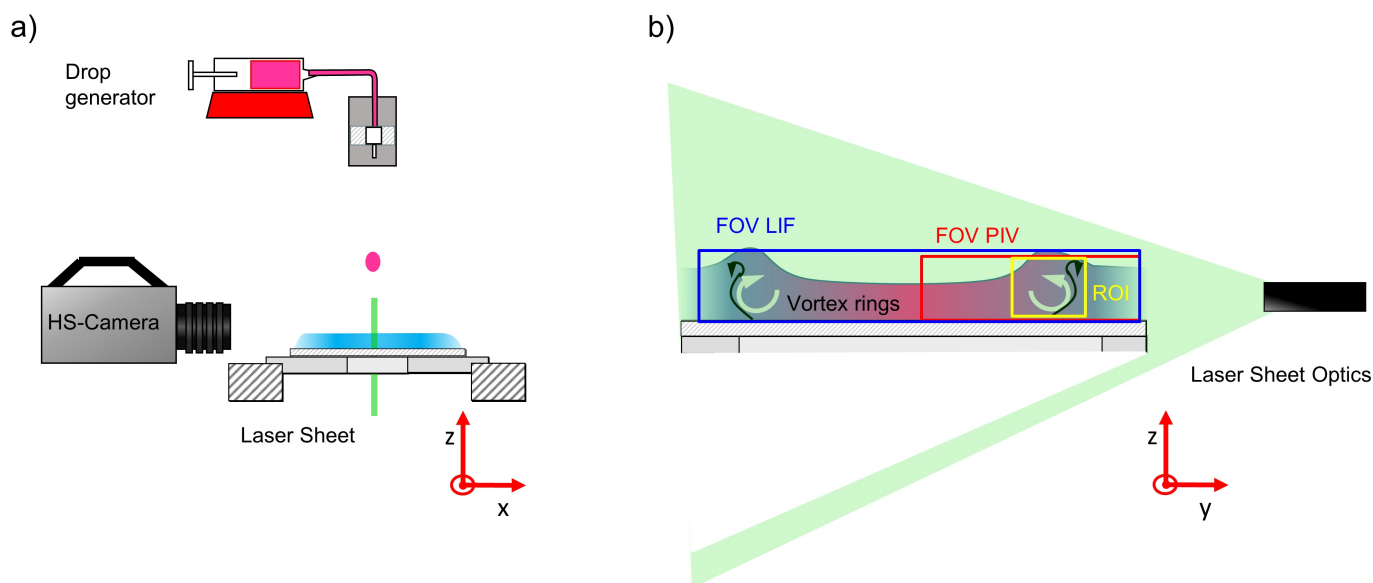


**Figure 2.** Schematic illustration of side view setup.

The side view setup employs the same drop generator configuration as the bottom view. The impact substrate part is also similar, with the primary difference being the use of fluorescent dye. For the side view setup, the droplet itself is dyed with Rhodamine 6G for Laser-Induced Fluorescence (LIF) measurements. For Particle Image Velocimetry (PIV) measurements,  $10$   $\mu$ m glass beads are added to both the liquid film and the droplet. A high speed camera (Photron Fastcam Mini-AX200) and a  $532$  nm green light laser (Microvec) are used.

### 3. Method

To investigate the spatial and temporal evolution of vortex rings during droplet impact on thin liquid films, Particle Image Velocimetry (PIV) measurements were performed. Depending on the impact velocity and the thickness of the film, the high-speed camera operated at three different

frame rates: 10000, 8100, and 6400 fps. The captured images were processed using *LaVision DaVis 10.2* software, with interrogation windows of  $24 \times 24$  pixels and 75% overlap.

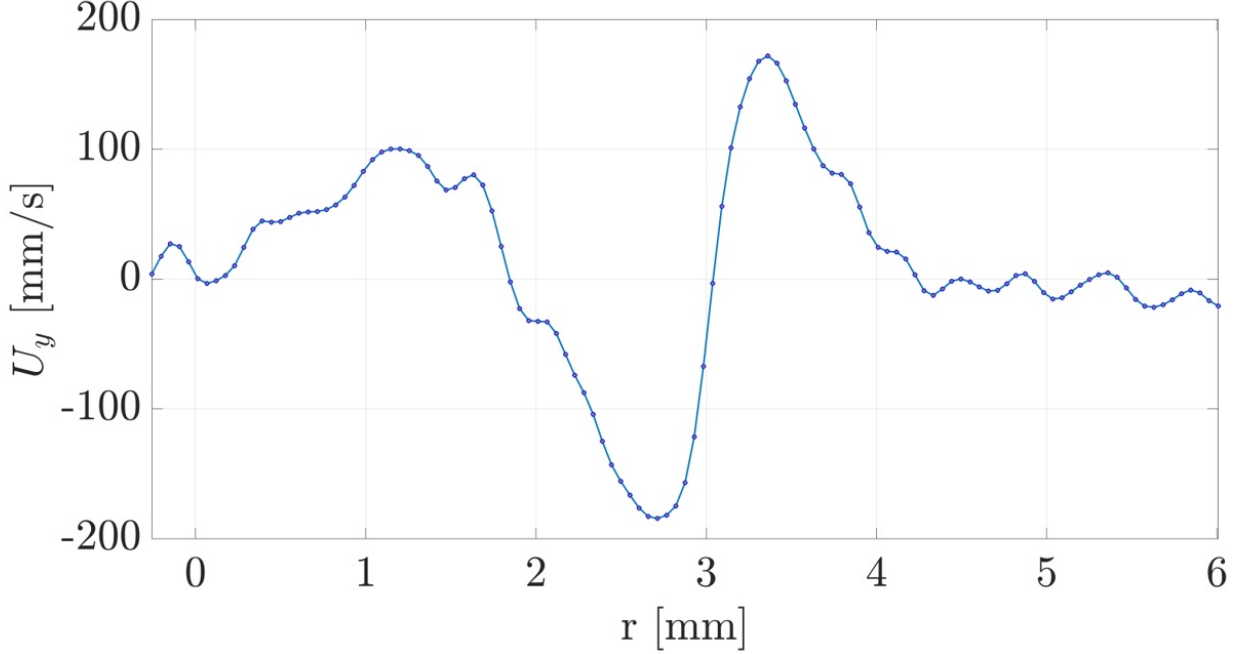


**Figure 3.** tangential velocity profile measured along a horizontal line passing through the centers of the vortex pair for  $\delta = 0.90$ ,  $We = 54$  and  $Re = 3900$  at  $t = 27$  ms.

The identification of the vortex center is crucial for extracting the circulation and position of the vortex, which are key parameters for investigating vortex behavior during droplet impact. For this purpose, the  $\Gamma_2$  scalar function, which is Galilean invariant, was employed. This method offers a reliable way to identify vortex centers, providing a robust measure of the vortex's core location (Kissing et al., 2021).

As described by Graftieaux et al. (2001), the  $\Gamma_2$  function is defined as follows:

$$\Gamma_2(P) = \frac{1}{S} \int_S \frac{[P\vec{M} \times (\vec{U}_M - \vec{U}_P)] \cdot \vec{z}}{\|P\vec{M}\| \cdot \|\vec{U}_M - \vec{U}_P\|} dS \quad (1)$$

where  $S$  is a two-dimensional area surrounding point  $P$ ,  $M$  is a point within  $S$ , and  $\vec{z}$  is the unit vector normal to the measurement plane. The term  $P\vec{M}$  represents the radius vector from  $P$  to  $M$ ,  $\vec{U}_M$  is the velocity vector at point  $M$ , and  $\vec{U}_P$  is the local convection velocity around  $P$ , defined as:

$$\vec{U}_P = \frac{1}{S} \int_S \vec{U} dS \quad (2)$$

Since PIV measurements involve sampling the velocity field at specific discrete points, the region  $S$  is defined as a rectangular area of fixed size centered around the point  $P$  (Graftieaux et al., 2001).  $\Gamma_2$  is then approximated by summing over discrete spatial locations within  $S$ :

$$\Gamma_2(P) = \frac{1}{N} \sum_S \frac{[P\vec{M} \times (\vec{U}_M - \vec{U}_P)] \cdot \vec{z}}{\|P\vec{M}\| \cdot \|\vec{U}_M - \vec{U}_P\|}, \quad (3)$$

where  $N$  represents the number of points  $M$  inside  $S$ . The location of the vortex center is determined by finding the local maximum of  $\Gamma_2$ , which reaches values between 0.9 and 1 near the vortex center.

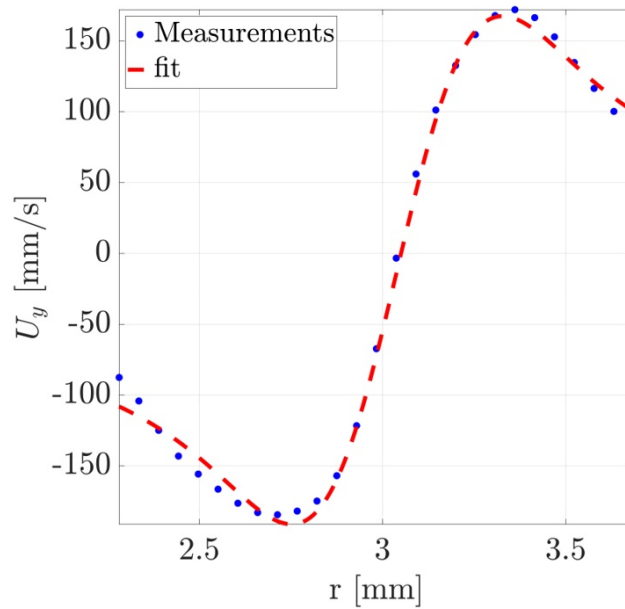


**Figure 4.** Least-squares fit of azimuthal velocities of two superposed Lamb-Oseen vortices (red line) and tangential velocity profile measured along a horizontal line passing through the centers of the vortex pair for  $\delta = 0.90$ ,  $We = 54$  and  $Re = 3900$  at  $t = 27$  ms (blue dots).

The circulation of vortex rings during the droplet impact was calculated by fitting the velocity profiles to the model of a Lamb-Oseen vortex, following methods similar to those described by Harris & Williamson (2012) and Leweke & Williamson (1998). As the vortex ring descends after the impact, the tangential velocity profile is measured along a horizontal line passing through the centers of the vortex pair (see Fig. 3). It can be described by the superposition of two Lamb-Oseen vortices, each with an azimuthal velocity profile:

$$\begin{cases} u_\phi(r_1) = \frac{\Gamma}{2\pi r_1} \left(1 - \exp\left(-\frac{r_1^2}{a^2}\right)\right), \text{ right vortex} \\ u_\phi(r_2) = \frac{-\Gamma}{2\pi r_2} \left(1 - \exp\left(-\frac{r_2^2}{a^2}\right)\right), \text{ left vortex} \end{cases} \quad (4)$$

where  $\Gamma$  is the circulation of the vortex,  $r_1$  and  $r_2$  are the radial distance from the vortex center, and  $a$  is a parameter characterizing the core size of the vortex. The velocity profile can then be represented by equation (5), where  $d$  is vortex ring inner diameter. A least-squares best-fit method is then employed to determine the circulation  $\Gamma$ , and core size  $a$  as shown in Fig. 4

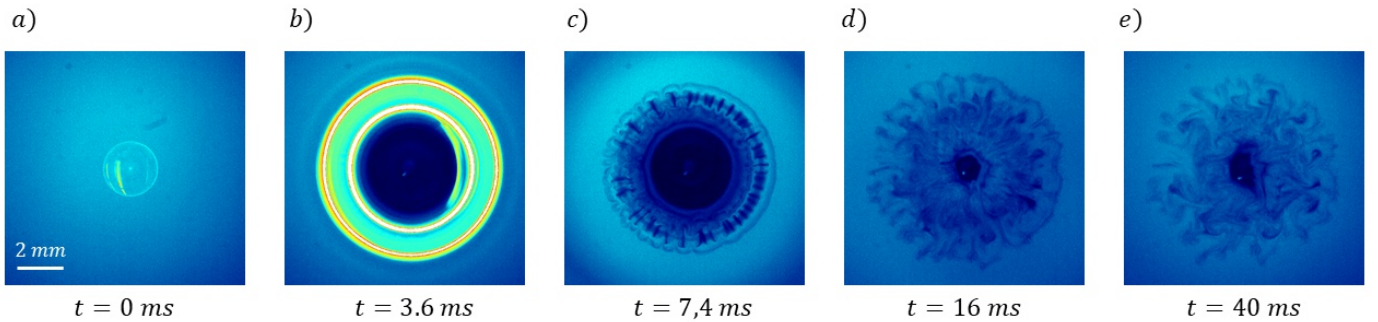
$$U_y(r) = \frac{\Gamma}{2\pi(r - d/2)} \left(1 - \exp\left(-\frac{(r - d/2)^2}{a^2}\right)\right) + \left(-\frac{\Gamma}{2\pi(r + d/2)}\right) \left(1 - \exp\left(-\frac{(r + d/2)^2}{a^2}\right)\right), \quad (5)$$

By employing these techniques, this study aims to provide a comprehensive understanding of vortex ring behavior during droplet impacts on thin liquid films.

#### 4. Results and Discussion

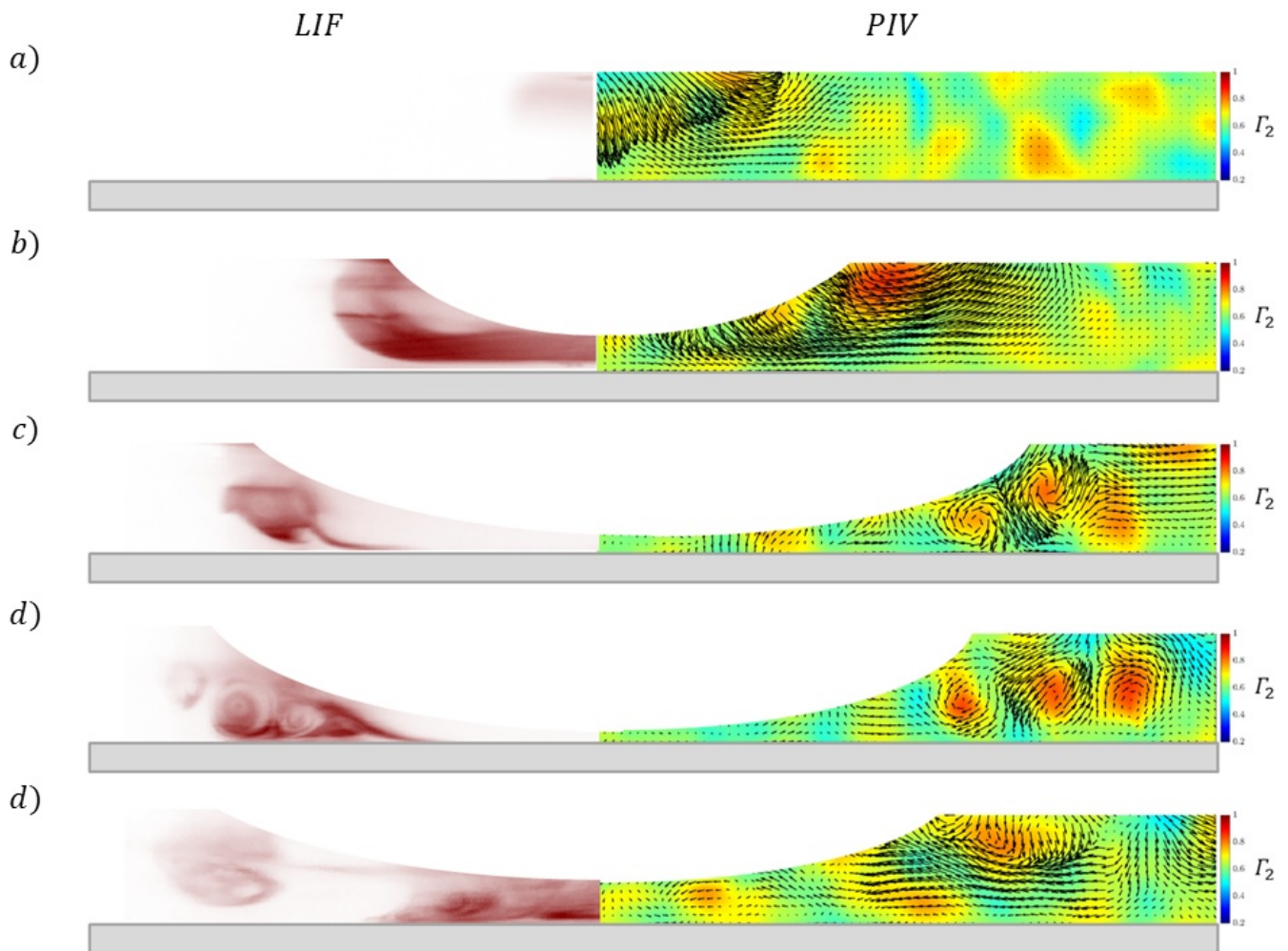
The results of this study highlight the instability of vortex rings generated during the impact of a droplet on a thin liquid film with a dimensionless thickness of  $\delta = 0.29$ , a Weber number ( $We$ ) of 54, and a Reynolds number ( $Re$ ) of 3900. This case is illustrated through a series of images captured from both bottom and side views, as shown in Figs. 5 and 6, respectively.

Fig. 5 presents a sequence of five images depicting the impact from the bottom view. At  $t = 0$  ms, the initial impact leads to the spreading of the droplet and the formation of a crater. This expanding crater has a remaining film thickness significantly lower than the initial film thickness prior to the droplet impact, resulting in low fluorescence intensity. In this study, the crater is defined by the circular region bounded by a steep gradient in the intensity signal.



**Figure 5.** Bottom view raw images of water droplet impact on fluorescent-labeled thin liquid film of thickness  $\delta = 0.29$  for  $we = 54$  and  $Re = 3900$ . **a**  $t = 0$  ms, **b**  $t = 3.6$  ms, **c**  $t = 7.4$  ms, **d**  $t = 16$  ms **e**  $t = 40$  ms.

Fig. 6 showcases the side view, with the left half displaying LIF measurements and the right half showing PIV measurements. The PIV measurements are color-coded using the  $\Gamma_2$  scalar, which defines the boundaries and centers of the vortices. At  $t = 3.6$  ms, the generated vortex can be spotted, which is indicated by the red region in Fig. 6b (right). At  $t = 7.4$  ms, the first instabilities in the vortex ring are observed, characterized by finger-shaped patterns, as shown in Fig. 5c. These instabilities are more clearly explained with the aid of the side view. Fig. 6c reveals the presence of two additional vortex rings that lead into azimuthal instabilities: a secondary vortex ring on the outside of the primary one and a smaller tertiary ring on the inside. This phenomenon is primarily attributed to the Kelvin-Helmholtz instability occurring during the spreading of the primary vortex ring and the droplet.



**Figure 6.** High-speed LIF visualizations (left) and  $\Gamma_2$  scalar field (right) during droplet impact onto thin liquid film of thickness  $\delta = 0.29$  for  $we = 54$  and  $Re = 3900$ . **a**  $t = 0$  ms, **b**  $t = 3.6$  ms, **c**  $t = 7.4$  ms, **d**  $t = 16$  ms **e**  $t = 40$  ms.

In Fig. 6, the formation of the three Vortices is clearly visible in both LIF and PIV measurements. The vortices then decay generating a turbulent mixing pattern as observed in Fig. 5e. This behavior is consistent with previous findings by Ennayar et al. (2023) regarding vortex ring instability

after wall impact. The observed instabilities in the vortex rings, as explained in section 1, result from a combination of long-wavelength perturbations (Crow instability (Crow, 1970)) and short-wavelength perturbations (Tsai-Widnall-Moore-Saffman instability or elliptical instability (Tsai & Widnall, 1976), (Moore & Saffman, 1975)).

The effect of film thickness on vortex ring dynamics was further investigated for different thicknesses. Fig. 7 illustrates a series of four images for two different thicknesses:  $\delta = 0.45$  (right) and  $\delta = 0.90$  (left) at the same  $We = 54$  and  $Re = 3900$  as the last example.

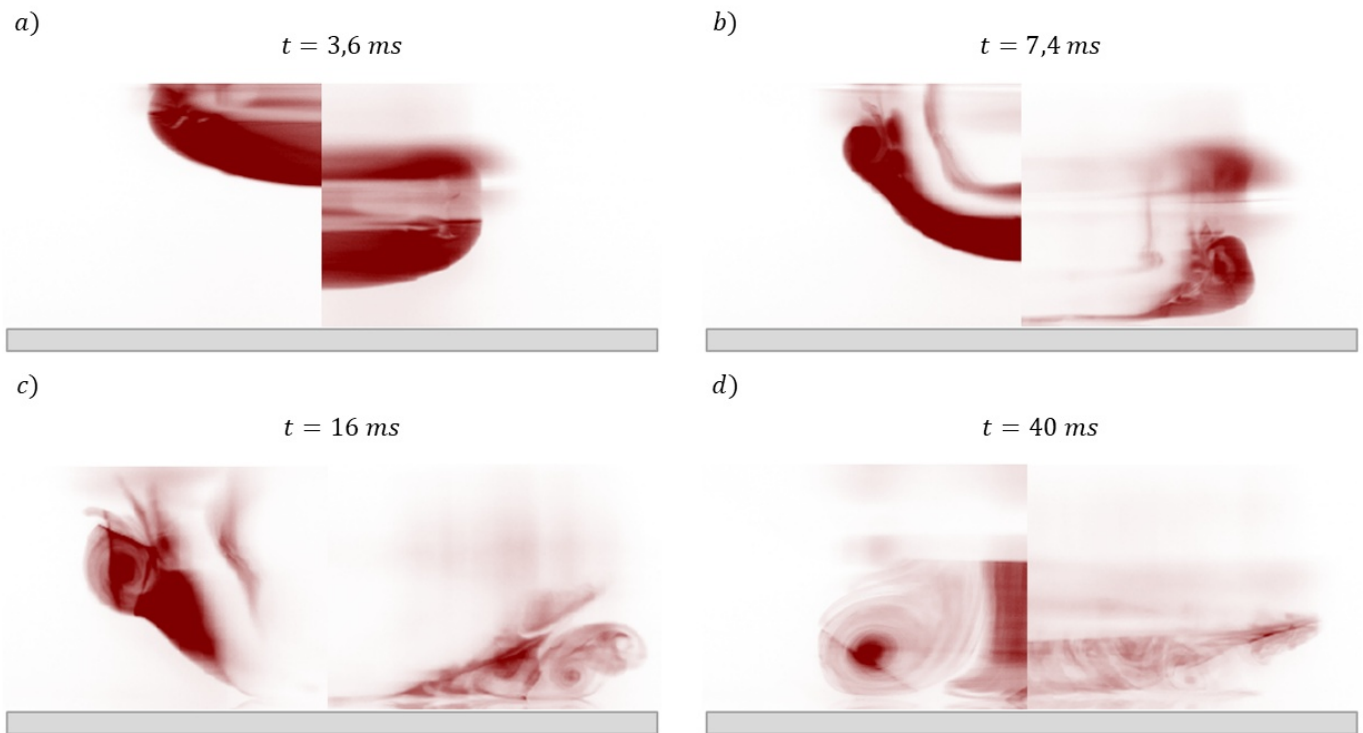


**Figure 7.** High-speed LIF visualizations during droplet impact onto thin liquid film of thickness  $\delta = 0.45$  (right) and  $\delta = 0.90$  left. **a**  $t = 3.6$  ms, **b**  $t = 7.4$  ms, **c**  $t = 16$  ms **d**  $t = 40$  ms.

At  $t = 3.6$  ms (Fig. 7a), the vortex rings for both  $\delta = 0.45$  and  $\delta = 0.90$  are observed to be similar size, penetrating the thin film. In contrast, for  $\delta = 0.29$  (see Fig. 6b), the vortex ring has already reached the wall and started expanding radially. By  $t = 7.4$  ms, the vortex ring for the case  $\delta = 0.45$  also reaches the wall and begins expanding radially as can be seen in Fig. 7b, whereas for  $\delta = 0.90$ , the vortex ring continues to sink deeper into the film, only reaching the wall at  $t = 25$  ms and without showing any signs of instability as can be observed at  $t = 40$  ms (Fig. 7d). The  $\delta = 0.45$  case experiences a lift-off of the boundary layer, which leads into a secondary vortex, and subsequently a turbulent mixing as depicted in Fig. 7d. A key difference between  $\delta = 0.45$  and  $\delta = 0.29$  is the absence of a tertiary vortex ring. This can be attributed to the lack of sufficient kinetic energy to trigger the Kelvin-Helmholtz instability for the formation of the third vortex ring, due to the greater distance between the thin film surface and the wall. The absence of instability in the case

of thicker film ( $\delta = 0.90$ ), on the other hand, can be explained by the vortex ring losing strength due to viscous forces while sinking through the film before colliding with the wall. This reduced strength prevents the development of instabilities that are otherwise observed in thinner films. This strength will be quantified in the next sections by the circulation of the vortex.

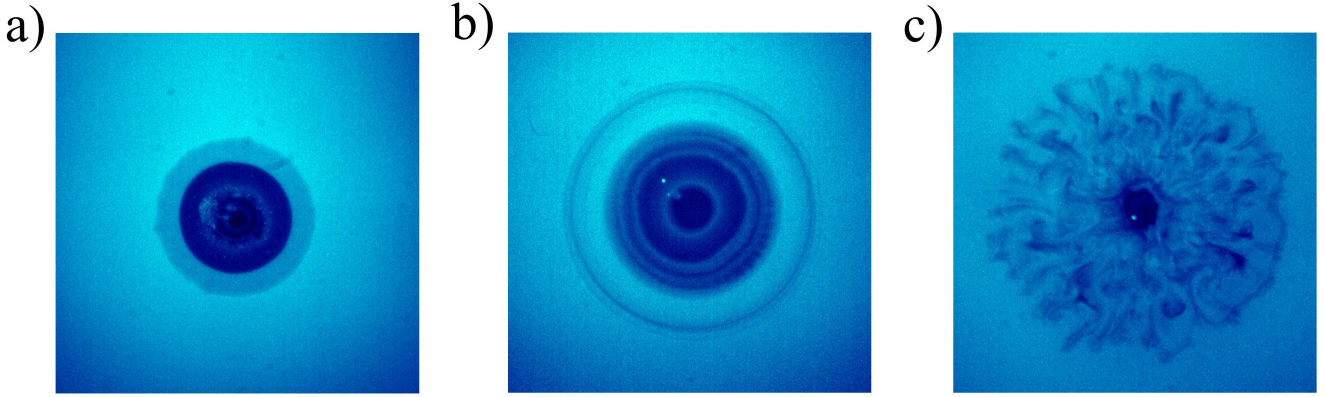


**Figure 8.** Vortex ring outcomes: a) spreading, b) multiple vortex rings and c) instability.

From the parameter study, which considered different droplet diameters, film thicknesses, and impact velocities, it was observed that the outcomes of vortex ring behavior vary depending on the impact energy and the dimensionless thickness, as shown in Fig. 8. The first observed outcome is the spreading of the vortex ring due to radial stretching following wall collision (Fig. 8a). With increased impact energy, the radial stretching intensifies, leading to the separation of the boundary layer near the wall. This flow separation due to the Kelvin-Helmholtz instability triggers the formation of additional vortex rings, which is evident in Fig. 8b. The generation of multiple vortex rings indicates a complex interaction where the initial ring's energy is assumed to dissipate through the creation of secondary structures. At even higher Reynolds numbers, the vortex ring undergoes significant azimuthal instabilities, resulting in turbulent mixing (Fig. 8c). These instabilities cause the vortex ring to break down into a turbulent cloud, demonstrating a high-energy dissipation process. Furthermore, Fig. 9 presents the results of experimental phase mapping examining the influence of Reynolds number  $Re$  and the dimensionless thickness  $\delta$  on the observed outcomes. The graph reveals a critical threshold, which can be approximated by Eq. (6), that shows the parameter range where instability occurs from not.

$$Re = 2141 - 14.71 \cdot \delta^{-3/2} \quad (6)$$

The analysis of the number of fingers resulting from the instability reveals a relationship between the number of fingers ( $F$ ) and the Reynolds number, given by:

$$F = B \cdot Re \quad (7)$$

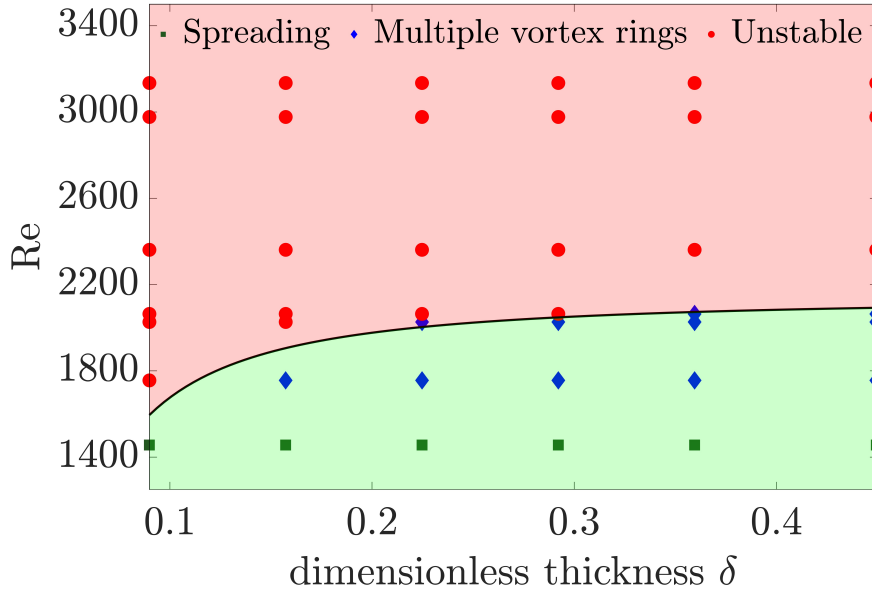


**Figure 9.** Influence of Reynolds number and dimensionless film thickness on instability.

The coefficient  $B$  depends on the dimensionless film thickness  $\delta$ . In Fig. 10a, The coefficient  $B$  is plotted against  $\delta$  for different  $Re$ . The figure also includes a scaling relation, approximated by Eq. (8), which demonstrates a good correlation between the coefficient  $B$  values obtained from Eq. (7) and those predicted by Eq. (8) for the investigated range of Reynolds number as can be seen in Fig. 10b. additionally, it is observed that the number of fingers increases with a decrease in film thickness and an increase in Reynolds number.

$$B = 0.02573 - 0.0334 \cdot \delta^{0.8398} \quad (8)$$

The final analysis focuses on the evolution of vortex circulation over time, as depicted in Fig. 11. The plot compares two cases:  $\delta = 0.90$  and  $\delta = 0.45$ . For both cases, it is observed that the circulation increases with time immediately after the droplet impact, indicating the generation of the vortex ring. Subsequently, a decrease in circulation is noted. For  $\delta = 0.45$ , there is a sharp decrease in circulation, which can be attributed to the dissipation of vortex energy into the generation of a secondary vortex ring. In contrast, for thicker films ( $\delta = 0.90$ ), the decrease in circulation occurs more gradually, primarily due to the viscous dissipation. Once the vortex ring reaches the wall at  $t = 25$  ms and settles, the decrease in circulation slows down further.

Notably, the circulation of the vortex ring for thinner films (i.e.  $\delta = 0.45$ ) is higher at the moment of collision with the wall compared to thicker films (i.e.  $\delta = 0.90$ ). This higher circulation at the point of impact with the wall explains the observed instability for thinner films, as the greater energy facilitates the formation of additional vortex structures and instabilities.

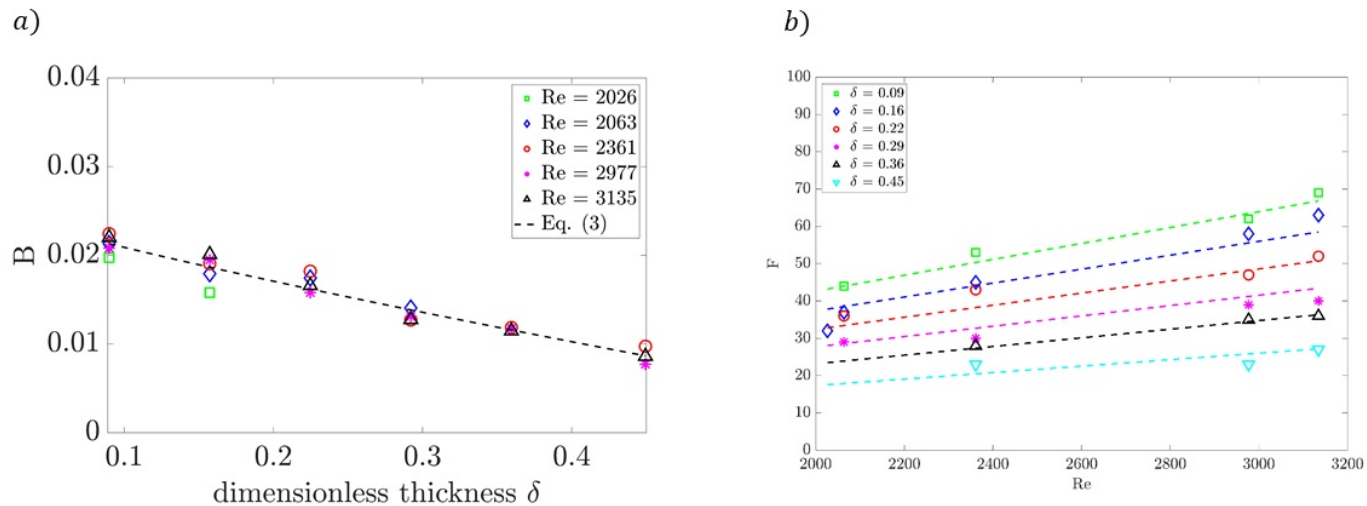


**Figure 10.** **a** Correlation between predicted and measured values of coefficient  $B$ , showing relationship between number of fingers and Reynolds number. **b** Experimentally and computationally obtained number of fingers during droplet impact on thin liquid film.

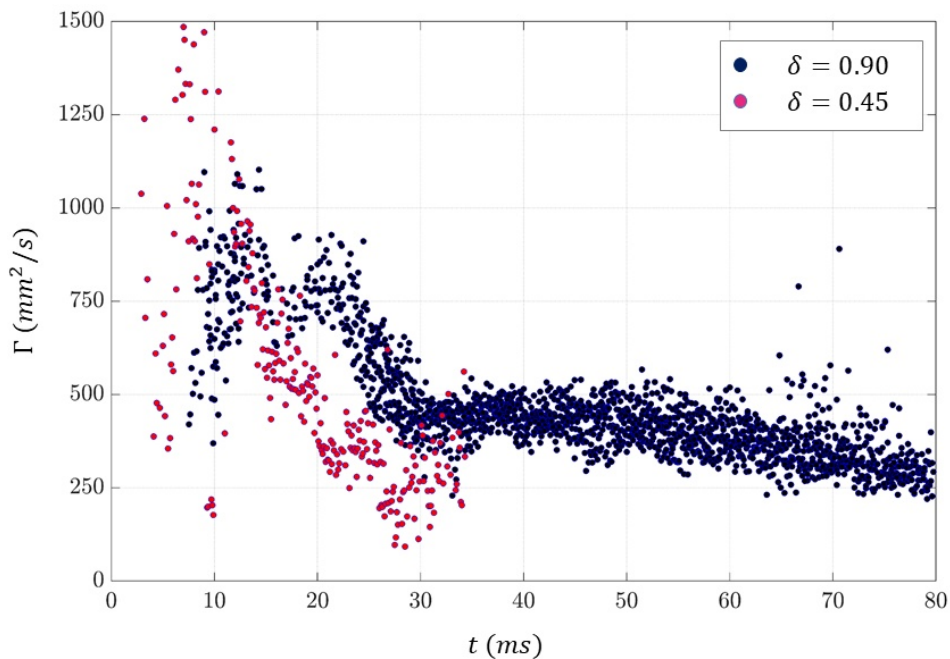


**Figure 11.** Time evolution of vortex circulation for two different dimensionless film thicknesses,  $\delta = 0.90$  (blue) and  $\delta = 0.45$  (pink).

## 5. Conclusions

This study presents a comprehensive analysis of vortex ring instabilities during droplet impacts on thin liquid films, utilizing high-speed PIV and LIF techniques. The findings underscore the significant influence of dimensionless film thickness ( $\delta$ ), Weber number ( $We$ ), and Reynolds number ( $Re$ ) on vortex ring behavior. Thinner films exhibit pronounced vortex instabilities, driven by higher energy dissipation upon wall collision, leading to the formation of secondary and tertiary vortex rings. Conversely, thicker films show a lack of vortex ring instability due to the lower strength of the vortex during the collision with the wall.

The identification of critical thresholds for vortex ring instability and the correlation between the number of fingers and  $Re$  provide valuable insights for controlling fluid dynamics in various applications, such as coating processes and microfluidics. The study's experimental phase mapping offers a predictive model for instability occurrence, enhancing the understanding of vortex ring-driven mixing processes.

Overall, this research contributes to the fundamental knowledge of vortex ring dynamics in thin liquid films during droplet impact, highlighting the intricate interplay between impact parameters and fluid behavior. Future work could extend these findings to more complex fluid systems.

## Acknowledgements

This project is funded by the Deutsche Forschungsgemeinschaft (DFG, German Research Foundation) – project number 237267381 – TRR 150, sub-project A07 and project number 265191195 – SFB 1194, sub-project A03.

## Nomenclature

$Re$	Reynolds number [-]
$We$	Weber number [-]
$D$	Droplet diameter [m]
$h$	Film thickness [m]
$\delta$	Dimensionless thickness [-]
$\lambda$	wavelength [m]
$\Gamma_2$	Vortex center identification scalar [-]
$\Gamma$	Vortex circulation [ $\text{m}^2 \text{s}^{-1}$ ]
$U$	Velocity [ $\text{m s}^{-1}$ ]
$x, y, z$	Cartesian coordinates [m]
$r, r_1, r_2$	Radial position [m]

$a$	Vortex core size [m]
$d$	Vortex ring inner diameter [m]
$u_\phi$	Tangential velocity [ $\text{m s}^{-1}$ ]
$t$	Time [s]
$F$	Number of fingers [-]

## References

- Archer, P., Thomas, T., & Coleman, G. (2010). The instability of a vortex ring impinging on a free surface. *Journal of fluid mechanics*, 642, 79–94.
- Cheng, M., Lou, J., & Luo, L.-S. (2010). Numerical study of a vortex ring impacting a flat wall. *Journal of Fluid Mechanics*, 660, 430–455.
- Cresswell, R., & Morton, B. (1995). Drop-formed vortex rings—the generation of vorticity. *Physics of Fluids*, 7(6), 1363–1370.
- Crow, S. C. (1970). Stability theory for a pair of trailing vortices. *AIAA journal*, 8(12), 2172–2179.
- Ennayar, H., Brockmann, P., & Hussong, J. (2023). Lif-based quantification of the species transport during droplet impact onto thin liquid films: Species transport during droplet impact onto thin liquid films. *Experiments in Fluids*, 64(9), 148.
- Graftieaux, L., Michard, M., & Grosjean, N. (2001). Combining piv, pod and vortex identification algorithms for the study of unsteady turbulent swirling flows. *Measurement Science and technology*, 12(9), 1422.
- Harris, D., & Williamson, C. (2012). Instability of secondary vortices generated by a vortex pair in ground effect. *Journal of Fluid Mechanics*, 700, 148–186.
- Kissing, J., Stumpf, B., Kriegseis, J., Hussong, J., & Tropea, C. (2021). Delaying leading edge vortex detachment by plasma flow control at topologically critical locations. *Physical Review Fluids*, 6(2), 023101.
- Lee, J. S., Park, S. J., Lee, J. H., Weon, B. M., Fezzaa, K., & Je, J. H. (2015). Origin and dynamics of vortex rings in drop splashing. *Nature communications*, 6(1), 8187.
- Leweke, T., & Williamson, C. H. (1998). Cooperative elliptic instability of a vortex pair. *Journal of fluid mechanics*, 360, 85–119.

- Lim, T. (1997a). A note on the leapfrogging between two coaxial vortex rings at low Reynolds numbers. *Physics of Fluids*, 9(1), 239–241.
- Lim, T. (1997b). On the role of Kelvin-Helmholtz-like instability in the formation of turbulent vortex rings. *Fluid dynamics research*, 21(1), 47–56.
- McKeown, R., Ostilla-Mónico, R., Pumir, A., Brenner, M. P., & Rubinstein, S. M. (2020). Turbulence generation through an iterative cascade of the elliptical instability. *Science advances*, 6(9), eaaz2717.
- Mishra, A., Pumir, A., & Ostilla-Mónico, R. (2021). Instability and disintegration of vortex rings during head-on collisions and wall interactions. *Physical Review Fluids*, 6(10), 104702.
- Moore, D. W., & Saffman, P. G. (1975). The instability of a straight vortex filament in a strain field. *Proceedings of the Royal Society of London. A. Mathematical and Physical Sciences*, 346(1646), 413–425.
- Peck, B., & Sigurdson, L. (1994). The three-dimensional vortex structure of an impacting water drop. *Physics of Fluids*, 6(2), 564–576.
- Saha, A., Wei, Y., Tang, X., & Law, C. K. (2019). Kinematics of vortex ring generated by a drop upon impacting a liquid pool. *Journal of Fluid Mechanics*, 875, 842–853.
- Shariff, K., & Leonard, A. (1992). Vortex rings. *Annual Review of Fluid Mechanics*, 24(1), 235–279.
- Thoraval, M.-J., Li, Y., & Thoroddsen, S. T. (2016). Vortex-ring-induced large bubble entrainment during drop impact. *Physical Review E*, 93(3), 033128.
- Tsai, C.-Y., & Widnall, S. E. (1976). The stability of short waves on a straight vortex filament in a weak externally imposed strain field. *Journal of Fluid Mechanics*, 73(4), 721–733.